PCCP

From graphene to graphene oxide: the importance of extended topological defects.

Journal:	*Physical Chemistry Chemical Physics*
Manuscript ID	CP-ART-09-2021-004316.R1
Article Type:	Paper
Date Submitted by the Author:	22-Dec-2021
Complete List of Authors:	Marsden, Alexander; University of Warwick, Physics Skilbeck, Mark; University of Warwick, Physics Healey, Matthew; University of Warwick, Physics Thomas, Helen; University of Warwick, Chemistry Walker, Marc; University of Warwick, Department of Physics Edwards, Rachel; University of Warwick, Physics Garcia, Natalya; Deakin University, Institute for Frontier Materials Vuković, Filip; Institute for Frontier Materials, Jabraoui, Hicham; Deakin University, Institute for Frontier Materials Rourke, Jonathan; University of Warwick, Chemistry Walsh, Tiffany; Deakin University, Institute for Frontier Materials Wilson, Neil; University of Warwick, Physics

SCHOLARONE™
Manuscripts

ARTICLE

From graphene to graphene oxide: the importance of extended topological defects.

Alexander J. Marsden[a], Mark Skilbeck[a], Matthew Healey[a], Helen R Thomas[b], Marc Walker[a], Rachel S. Edwards[a], Natalya A. Garcia[c], Filip Vuković[c], Hicham Jabraoui[c], Tiffany R. Walsh[c], Jonathan P Rourke[b*], Neil R. Wilson[a*]*

Graphene oxide (GO) represents a complex family of materials related to graphene: easy to produce in large quantities, easy to process, and convenient to use as a basis for further functionalization, with the potential for wide-ranging applications such as in nanocomposites, electronic inks, biosensors and more. Despite their importance, the key structural traits of GO, and the impact of these traits on properties, are still poorly understood due to the inherently berthollide character of GO which complicates the establishment of clear structure/property relationships. Widely accepted structural models of GO frequently neglect the presence of extended topological defects, structural changes to the graphene basal plane that are not removed by reduction methods. Here, a combination of experimental approaches and molecular simulations demonstrate that extended topological defects are a common feature across GO and that the presence of these defects strongly influences the properties of GO. We show that these extended topological defects are produced following even controlled 'gentle' functionalization by atomic oxygen and are comparable to those obtained by a conventional modified Hummers' method. The presence of the extended topological defects is shown to play an important role in the retention of oxygen functional groups after reduction. As an exemplar of their effect on the physical properties, we show that the GO sheets display a dramatic decrease in strength and stiffness relative to graphene and, due to the presence of extended structural defects, no improvement is seen in the mechanical properties after reduction. These findings indicate the importance of extended topological defects to the structure and properties of functionalized graphene, which merits their inclusion as a key trait in simple structural models of GO.

1. Introduction

The perfect 2D hexagonal lattice of carbon atoms in graphene is responsible for its most celebrated properties: massless Dirac fermions and superlative mechanical strength.[1] While it is possible to grow or mechanically exfoliate perfect sheets of graphene, these are normally of restricted size and available in limited quantities, thus constraining their use.[2] Hence there has been an emphasis on liquid-phase exfoliation of graphite and the use of graphene oxide (GO) and reduced GO (rGO).[3,4] On the face of it, GO and rGO offer many advantages over pristine graphene: they can be made in large (multigram) quantities, they can be processed in solution and they are easily chemically functionalized.[5–7] However, the electrical and mechanical properties of GO and rGO are significantly degraded relative to graphene, due to the significant changes in the chemical and physical structure accompanying the conversion from graphene to GO.

Controversy surrounded the molecular structure of GO for many years, with a number of competing molecular models.[6–12] Although it is acknowledged that the exact structure is dependent on the reaction conditions, the Lerf-Klinowski model is regarded as the most appropriate simple model of GO,[9,10] though even that model has been adapted in the light of the more recent discovery of the presence of oxidative debris (OD) that decorate the surface.[13,14] The Lerf-Klinowski model is based on graphene-like sheets that are randomly functionalised across the surface with hydroxyl and epoxide groups, together with carboxyl and ketone groups at sheet edges.

Other adaptations of this model distinguish between in-plane oxygen functionalisation (e.g. carbonyls at the edge) and on-plane functionalisation (e.g. epoxides bridging two carbons within the plane), although it is difficult to distinguish between the two using standard analytical techniques.[6,12] Further distinctions can be made with carbon-based defects: vacancy defects (atoms missing from the plane, which may evolve into larger holes) and subsequent topological defects such as Stone-Wales defects[15] (which arise from rotation of bonds within the lattice).

Most evidence points to very low levels of defects in graphene derived from graphite so, to a first approximation, we can assume all defects in GO and rGO arise from the oxidation, workup, and imaging procedures used, as well as the

[a]Department of Physics, University of Warwick, Coventry, CV4 7AL, U.K.
[b]Department of Chemistry, University of Warwick, Coventry, CV4 7AL, U.K.
[×]Institute for Frontier Materials, Deakin University, Geelong VIC, 3216, Australia
Electronic Supplementary Information (ESI) available: further details on the XPS and Raman spectra; selected area diffraction patterns; molecular dynamics simulations: computational details; measuring mechanical properties by AFM. See DOI: 10.1039/x0xx00000x

subsequent reduction from GO to rGO. All defects, whether they be oxygenation (in- or on-plane), vacancy or topological, result in areas that are locally more reactive than a pristine carbon lattice, thus inevitably leading to clustering of defects and eventually more extended defect arrays.

Fundamentally, though, GO is based on a defective graphene-like structure and it is pertinent to ask how and when the various defects arise, how they evolve, and how they affect the properties. Specifically, although the concept of the extended topological defect (ETD) in GO is not new, an explanation of its origins, its prevalence in GO as a function of oxidation process, and its impact on the properties of GO is not well understood. Previously we have examined low levels of oxygen functionalisation of graphene by exposure to atomic oxygen;[16] here we extend the study to look at how a GO-like structure could be formed from graphene. High-resolution transmission electron microscopy (HRTEM) and scanning transmission electron microscopy (STEM), provide powerful methods of characterisation, as they allows for the direct visualisation of a graphene or GO surface[12,17–21] and, using STEM with electron energy-loss spectroscopy (EELS), local chemical analysis.[22,23] Prior HRTEM work on rGO has shown defects in the graphene basal plane,[18] that these defects are often clustered into extended topological defects (ETDs)[17] and that holes are present in the graphene films. The presence of ETDs and holes is crucial to the understanding of GO, as simple reduction and annealing processes cannot repair such features to regenerate a perfect graphene sheet without the use of high temperature graphene etching and growth conditions.[24,25]

The question becomes: how and when do these defects appear? Are they intrinsic to GO or are they caused by the reduction process or, are they simply artefacts of the imaging process and caused by the effects of the electron beam? And once defects are established as part of the GO structure, how do they affect the distribution and retention of oxygen bearing groups? To date only limited experimental data have been recorded. There is some evidence that GO will retain oxygen even when highly reduced[26,27]; however, other experiments suggest the possibility of converting GO to graphene via defect repair by chemical vapour deposition[27,28]. Computational approaches to study the relative stability of various defects[29,30] have led to suggestions as to how these defects might evolve. Although density functional theory (DFT) calculations have been useful for studying point defects and functional groups typical to GO[31–36], these have been limited to both small length-scales and short time-scales. As an alternative, ReaxFF is a bond order-based force field capable of describing covalent bond formation and disassociation, and based upon its current parametrization, could be used to explore annealing of GO over greater time- and length-scales. The ReaxFF potential has previously produced simulation data of GO consistent with experiment *e.g.* to examine how defects arise,[37–40] and how the initial distribution of oxygen-bearing functional groups affects the GO structure.[41–44] However, these previous studies were based on initial GO structures comprising an intact carbon lattice decorated with oxygen functional groups, which could then probe the subsequent evolution of defective carbon lattice structures.

[37,38,41,42] A current knowledge gap exists concerning the examination of how these GO structures evolve in the presence of ETDs, which would model the influence of vacancy and topological defects that are present from the outset.

To answer all these questions, we study the evolution of the atomic structure of graphene upon extended exposure to atomic oxygen and make comparisons with the effect of reduction on GO and explore possible structural consequences using computational molecular dynamics (MD) simulations. Thus, pristine CVD-grown graphene was exposed to atomic oxygen, and GO was reduced through a combination of chemical and heat treatments and their atomic structure determined by low-dose HRTEM. Atomic force microscopy (AFM) was used to test the mechanical properties, measuring the Young's modulus and the breaking strength of the sheet. In parallel, the evolution of the structure of oxygen functionalities and carbon centred defects in GO was explored using MD simulations to investigate both structure and resultant chemical properties.

Our results show that atomic oxygen functionalisation ultimately causes irreversible extended topological defects in the graphene lattice and there comes a point where oxidative treatment of graphene gives a material indistinguishable from GO. Furthermore, these extended topological defects have profound effects upon the properties of the GO sheet, distinguishing them from graphene.

2. Methods

2.1 Graphene chemical vapour deposition. As previously reported,[16,45] copper foils s (99.5% purity, 0.025 mm thick, Alfa Aesar product number 46365) were electropolished using a solution of orthophosphoric acid, urea, isopropanol, methanol and water, and then rinsed in water and isopropanol. The foils were sonicated in acetone, rinsed in isopropanol, and dried with nitrogen. They were then placed inside a 1-inch diameter quartz tube in a tube furnace. Graphene growth proceeded by low-pressure chemical vapour deposition (CVD), at a pressure of <100 mTorr. The foil was heated to 1000 °C over 20 minutes with a flow of hydrogen for 20 minutes, prior to the introduction of methane at 20 sccm for 20 minutes. The methane and hydrogen were kept on as the foil was cooled to 600 °C, after which the methane flow was stopped. SEM, TEM and Raman spectroscopy show that the graphene is predominantly monolayer, and is free from grain boundary defects.[45]

2.2 Graphene transfer. Graphene was transferred from the copper foils onto TEM grids or silicon substrates. The graphene-coated foils were coated with a thin layer of formvar by spin-coating. These stacks were placed on an ammonia persulphate solution to etch away the copper, leaving the formvar on graphene film floating on the surface. After etching, the stacks were washed by being transferred to de-ionised water 5 times and scooped onto either a silicon substrate or a silicon nitride TEM support grid containing an array of regularly spaced holes

with diameters of 3.25 μm and centre-centre distances of 6.5 μm (from Silson Ltd). For cleaning, the silicon substrates were soaked in chloroform for 5 minutes, acetone for 5 mins and then rinsed in isopropanol and dried in nitrogen. For the TEM grids, the same procedure was followed but instead of rinsing in isopropanol, they were dried in a critical point dryer using liquid CO_2 to preserve the free-standing film.

2.3 Atomic oxygen dosing. Graphene on copper foil, or after transfer to TEM grids or silicon, was introduced into ultrahigh vacuum (UHV, <10^{-8}mbar). A TC150 gas cracker (50 W) was used to crack oxygen into atomic species that are incident at low energy on to the surface.

2.4 Preparation of graphene oxide. Graphene oxide was prepared using a modified Hummers method[46] as reported previously,[47] yielding as produced GO (aGO). The oxidative debris was removed by washing in NaOH, yielding bwGO.[13,14] GO (0.1 mg ml^{-1}). For Raman spectroscopy, bwGO was then spin-coated (3000 rpm, 0.1 s ramp) onto silicon substrates. For TEM, grids were plasma cleaned (100 W for 1 min) before a drop of GO (0.01 mg ml^{-1}) was cast onto the surface. To reduce the GO, samples were exposed to hydrazine vapours for 2 hours (yielding reduced GO, rGO),[48,49] followed by heating for 1 hour in air at 200 °C (yielding heated-reduced GO, hrGO).

2.5 X-ray photoelectron spectroscopy. X-ray photoelectron spectra were acquired with an Omicron XPS system with a monochromated Al Kα source operated under UHV, with the samples transferred in UHV directly into the XPS analysis chamber after exposure to atomic oxygen.

2.6 Raman spectroscopy. Raman spectra were acquired using a Renishaw InVia with a HeNe 633 nm laser. For graphene on copper, there is a broad background caused by fluorescence of the copper which has been removed using a 2nd order polynomial fit.

2.7 Transmission electron microscopy. For high-resolution imaging, a JEOL ARM 200F was used with operating voltage of 80 kV. Sample dose was minimised using JEOL's Minimum Dose System, which allows sample focusing away from the region of interest.

2.8 Atomic force microscopy measurements of mechanical properties. All AFM data were acquired using an Asylum Research MFP3D-SA AFM with MikroMasch NSC18 tips (silicon tip with nominal normal spring constant of 2.8 Nm^{-1}, resonance frequency of 75 kHz, and tip radius of 8 nm) which were calibrated using the Sader method.[50] The graphene, or functionalised graphene, was suspended across circular holes with diameters of 3.25 μm in a silicon nitride support membrane. The centre of each hole was found by imaging in AC mode (tapping mode) and force-distance curves acquired at the centre point. The force-distance curves were acquired with sequentially increasing maximum load force until the membrane was observed to break. The breaking load was determined from the highest load reached before breaking. The curve from the approach direction up to the breaking point was transformed to force versus indentation and corrected for

offsets and the resultant force versus indentation curve was fit to extract the 2D elastic modulus and pretension of the membrane. Provided the radius of the AFM tip is significantly smaller than the radius of the hole ($r_{tip} \ll r_{hole}$) and acting close to the centre of the hole, the system can be modelled as a point load acting on a clamped circular membrane of linear (i.e. no bending stiffness) isotropic elastic material. This model can be used to approximate the force-indentation (F-d) relationship as[51]

$$F = \sigma_{2D}^0 (2\pi r_{hole}) \left(\frac{d}{2r_{hole}}\right) + E_{2D}\left(2q^3 r_{hole}\right)\left(\frac{d}{2r_{hole}}\right)^3,$$

where σ_{2D}^0 is the pretension and E_{2D} is the 2D elastic modulus. E_{2D} is analogous to the Young's modulus of a 3D material and can be converted to an equivalent Young's modulus by dividing by the thickness of the sheet — for graphene the interplanar distance of graphite, 0.335 nm, was used and this is plotted in Figure 5 along with the 2D elastic modulus. Note that the layer thickness increases in GO and is typically taken to be around 1 nm. The dimensionless parameter, q, is given by $q = \left(1.05 - 0.15\nu - 0.16\nu^2\right)^{-1}$, where ν is the Poisson ratio. For graphene the Poisson ration can be taken as the in-plane Poisson ratio for graphite, 0.165, giving q = 1.02. Example force-curves are given in SI section SI4.

2.9 Molecular simulations. The molecular dynamics simulations considered four types of GO sheets as initial configurations, namely GO with an intact perfect carbon lattice, i.e. no defect or topological vacancies (GO-N), GO with decorated defect vacancies (GO-V), GO with topological defects (GO-T), and GO with both vacancy and topological defects (GO-TV).

In each case, a single graphene sheet was functionalized with ~30% oxygen in a ratio of 2:1 hydroxyl and epoxide groups on both the upper and low sides of the substrate. To produce approximate structural models of hrGO, the sheets were equilibrated at room temperature, followed by annealing to a temperature of T = 600, 900, 1200, or 2500 K, and held at this temperature for the remainder of the simulation. Although these temperatures exceed those used in the experimental heating protocol, the exploitation of the Arrhenius-like behaviour of the time-temperature relationship for carbon based materials[52,53] is common practise to make simulations computationally tractable, including with simulations specifically using ReaxFF.[37,42]

All sheet types had surface dimensions ~9.9x8.8x6.3nm^3, comprising 3444, 3409, 3444 and 3409 carbon atoms respectively. The GO-V and GO-TV samples had a total of 35 carbon atoms deleted from the pristine graphene 2D network, which were distributed over six holes of sizes 10, 7, 5, 5, 5 and 3 missing carbon atoms. The oxygen-bearing content of all systems comprised ~ 166 hydroxyl groups and ~129 epoxide groups. Of this total number of hydroxyl groups, 30% were configured as isolated hydroxyls, with the remaining 70% as dihydroxyls. Epoxide and hydroxyls were randomly distributed on both sides of the sheet. The exclusion of initial carboxyl groups was intentional and allowed for the objective
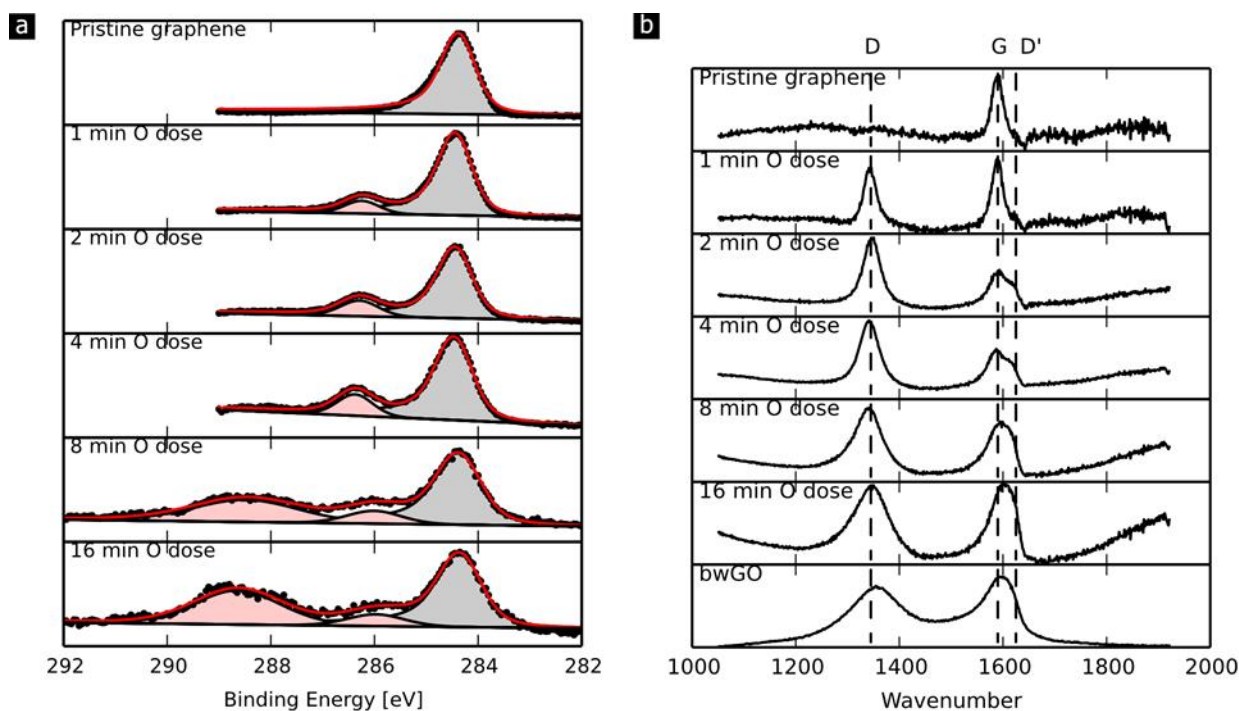
Figure 1. XPS and Raman spectroscopy of atomic oxygen functionalised graphene and GO. a) C1s XPS spectra for graphene with different times of exposure to atomic oxygen, the red line is the fit to the data with the fitted peaks shown as black lines with shading beneath. b) Raman spectra, the dashed lines indicate the positions of the D, G and D' peaks.

monitoring of defect-induced chemical conversion of existing hydroxyl and epoxy groups during annealing.

To avoid possible artefacts arising due to use of periodic boundary conditions, the oxygen-bearing groups were distributed in the centre of the sheet within a circle of diameter ~6.0 nm. The clustering of these defects within this region was deliberate; first to model co-location of these ETDs, and second, to ensure that the graphene lattice at the periodic boundary edges was minimally affected by sheet corrugation induced by the ETDs.

Simulations were performed using the LAMMPS software package.[54] All simulations were performed using 3D periodic boundary conditions and an integration time step of 0.1 fs. To describe the chemical mechanisms during the heating of the GO structures, the ReaxFF was used.[55–57] Following geometry optimization, the systems were brought to 300 K over 100 ps, and subsequently annealed at an upper temperature (600 K, 900 K, 1200 K or 2500 K) for a further 100 ps, all within the isothermal-isobaric ensemble to ensure that no residual stresses due to oxygen functionalisation were introduced. Full details, including the stress-strain simulations and calculations are provided in the SI, "Computational Details."

3. Results and discussion

CVD graphene was dosed with atomic oxygen in ultrahigh vacuum. Gas phase functionalisation allows easy control over the extent of the reaction by varying the exposure time and exposure to atomic oxygen (the highly reactive monoatomic oxygen radical formed by cracking diatomic oxygen) avoids damage due to the high energies usually found in plasma sources.

XPS spectra, Figure 1a, show that at low levels of functionalisation (between 1 and 4 minutes) the atomic oxygen forms epoxide groups on the graphene surface, without damage to the graphene lattice, consistent with previous reports on exposing graphene to atomic oxygen.[16,58] This is evident from the increasing intensity of the peak at 286.3±0.1 eV, corresponding to carbon in an epoxide group, alongside the peak at 284.4±0.1 eV associated with graphene. For doses greater than 4 minutes there is a change in the oxygen chemical environments: the epoxides remain but are joined by carboxyl and carbonyl groups (broad peak at 288.5±0.1 eV). Concomitant with this, there is a decrease in the total intensity of the carbon peaks, suggesting some removal of carbon from the graphene lattice. A more detailed discussion of the XPS spectra is given in Electronic Supplementary Information, ESI, section 1.

Raman spectra from graphene before and after oxygen functionalisation are shown in Figure 1b. For pristine graphene on copper, a single peak is observed at 1590 cm^{-1} which can be assigned to the G band of graphene. There are no other peaks in this region, including around 1345 cm^{-1} where the D-peak would be expected, indicating the graphene is free from disorder, typical for high-quality CVD graphene. After 1-minute of atomic oxygen dosing, the D-peak at 1345 cm^{-1} is already of similar intensity to the G-peak. After longer exposures to atomic oxygen, the D' peak at 1650 cm^{-1} emerges as well. Both D and D' peak are related to disorder in the graphene lattice[59]. After >4 minutes exposure to atomic oxygen, the G and D' peaks become too broad to be distinguished by eye and after 16 minutes of atomic oxygen dosing the Raman spectrum closely resembles that from base-washed graphene oxide (bwGO), suggesting comparable disorder to the graphene lattice.
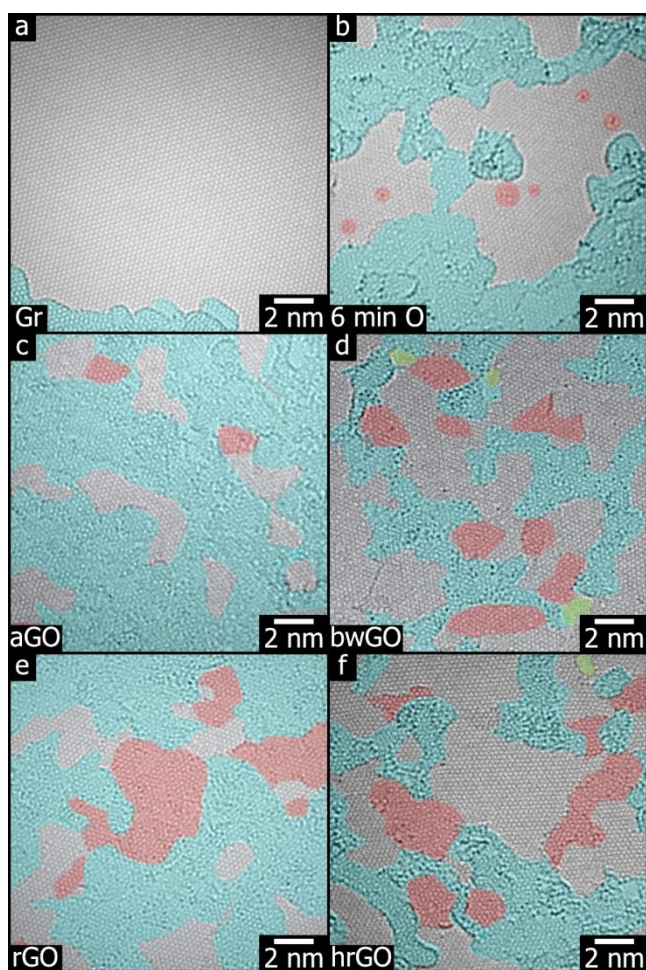
Figure 2. Aberration corrected transmission electron microscopy (acTEM) from graphene and graphene oxide. Panel (a) shows pristine graphene, with transfer residue highlighted in blue. Panel (b) shows graphene after exposure to atomic oxygen. Along with transfer residue (blue) there is also the presence of defects in the graphene lattice (red), caused by the oxygen dosing. Panel (c) shows as-produced GO (aGO), where the majority of the graphene lattice is covered in amorphous material (blue). Panel (d) shows base-washed GO (bwGO), which has significantly less amorphous material. The removal of amorphous material reveals extended defects (red) and holes in the lattice (green). Panel (e) shows reduced GO (rGO), and (f) heated-reduced GO (hrGO). These treatments have further reduced the amorphous material and again show the presence of defects.

Raman spectroscopy and XPS thus give indirect evidence that, despite the soft functionalisation approach, higher levels of functionalisation result in damage to the graphene lattice, giving spectra similar to those from graphene oxide synthesized by conventional wet chemical approaches. But these spectroscopic investigations do not directly reveal the resultant changes in atomic structure.

3.1 Physical structure of functionalized graphene. Insight into the structure of oxygen functionalised graphene can be provided by aberration corrected transmission electron microscopy (acTEM). Figure 2 compares acTEM images from graphene, both before and after controlled functionalization by exposure to atomic oxygen, as well as conventional GO, both before and after base-washing or reduction treatments. Sample fabrication details are given in the Methods. Importantly, TEM images were acquired at 80 kV using a minimum dose system that only exposes the image region to the electron beam for the

acquisition period, keeping the exposure down to 10 e$^-$ Å^{-2} before images are captured and hence minimizing the effect of electron beam damage.

Before functionalization, acTEM images of CVD graphene show a uniform hexagonal lattice across most of the image, Figure 2a. In the bottom left corner, highlighted in blue, is an amorphous region, likely to be polymer residue on the graphene that has not been removed after the transfer process[60] or adventitious carbon[47,61] from hydrocarbon contamination upon exposure to air. There are no defects visible in the lattice. Figure 2b shows graphene after a 6-minute oxygen dose. There are amorphous regions as before, which are again assigned to transfer residue and adventitious carbon. The apparent increase in amorphous regions is assigned primarily to more polymer transfer residue due to an accidentally more contaminated sample but may also be in part due to more adventitious carbon due to greater attraction to the functionalised regions. Along with the pristine graphene lattice there are now, highlighted in red, clusters of topological defects, where the hexagonal lattice is replaced by clusters of pentagons, heptagons and other irregular shapes, disrupting the lattice locally whilst the long-range order is still retained. Such extended topological defects induce in-plane and out-of-plane deformation of the graphene sheets[17] and cannot be removed by annealing or by standard chemical reduction procedures. To emphasize, these ETDs have arisen from the controlled functionalisation by atomic oxygen which at low functionalization levels (< 10%) is known to only cause reversible functionalisation by on-plane epoxide groups.[16,58]

Although acTEM gives detailed information on the lattice structure, our images do not reveal the sites of chemical functionalisation. We cannot distinguish between O and C in these images. Epoxide groups, which are still expected to be the dominant species at this level of functionalization, move quickly under the high-energy electron beam, or are removed by it, and so are not visible in the acTEM images.[16]

Figure 2c is an acTEM image from aGO. An FFT of this region shows a single set of hexagonal spots, demonstrating the long-range order in the graphene-lattice that forms the backbone of GO.[47] For aGO, although there is significantly more amorphous material than for graphene, there are regions of ordered graphene lattice and regions of ETDs. These images, acquired at low-dose and low-accelerating voltage to minimize damage due to the electron beam, demonstrate that ETDs are formed during the oxidation process. The appearance of ETDs is correlated here with the rise of the D' band in the Raman spectra of functionalised graphene, whether functionalized by controlled exposure to atomic oxygen or the conventional wet chemistry approach. Hence, we propose that the D' band in GO is associated with ETDs, giving a convenient signature of their presence.

Figure 2d shows atomic resolution images of bwGO. After base-washing, there is a reduction in the amount of amorphous material compared to aGO, suggesting that the oxidative debris adhered to the GO surface contributes to the amorphous regions observed in aGO. The bwGO also shows an increase in regions of ETDs compared to aGO. We suggest that removal of oxidative debris exposes disordered regions beneath, i.e. that
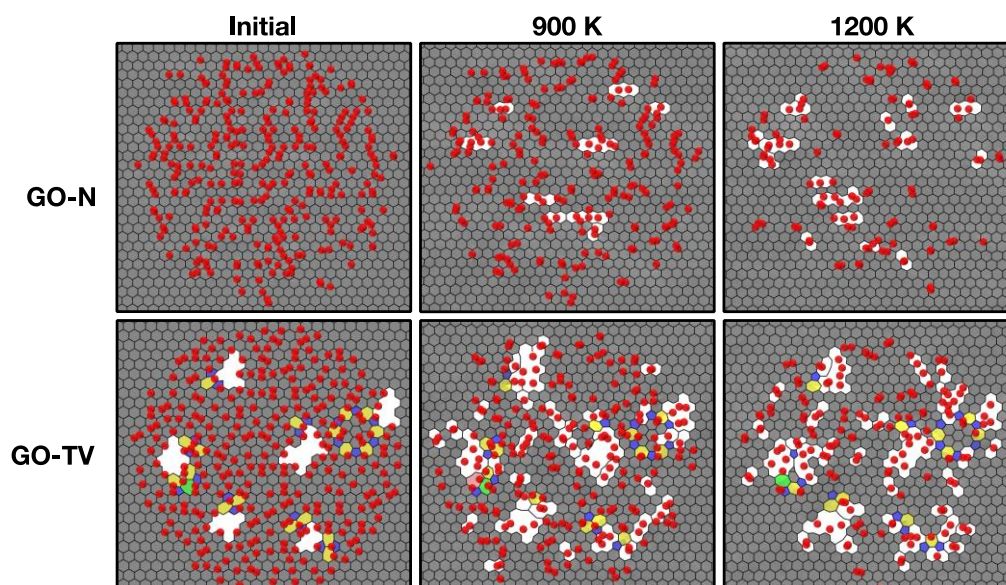
Figure 3. Top-down views of initial (pre-annealed) and final (post-annealed) graphene oxide lattice with (GO-N) no defects introduced and (GO-TV) both vacancy and topological defects introduced. Oxygen atoms are shown as red spheres. Rings are coloured according to ring size, r, with r = 5 (blue), 6 (grey), 7 (yellow), 8 (green), 9 (pink), >10 (white). Ring sizes larger than 10 have resulted either from the loss of carbon, or from lattice unzipping events, or both.

the OD preferentially complexes to the disordered regions, as others have suggested.[62] Finally, areas highlighted in green show no contrast, and are assigned to holes in the graphene sheet. Again, we expect that the holes are not caused by base-washing per se, but rather that they are hidden by the OD coverage on the aGO.

Figure 2e shows aGO after chemical reduction (rGO) and, Figure 2f, after chemical then heat treatment (hrGO). For rGO, there is less amorphous material than aGO, and an apparent increase in ETDs. For hrGO, there is an even stronger decrease in amorphous material and a clear increase in pristine graphene lattice regions. This suggests the reduction treatment has successfully removed much of the oxygen from the graphene lattice; however, there are still extensive regions of lattice defects. As discussed earlier, ETDs cannot easily be reversed to return to a pristine graphene lattice.

These results from atomically resolved images are corroborated by electron diffraction data, where the risk of electron beam damage is even lower. Small displacements away from the lattice-defined atomic positions, indicative of disorder due to thermal oscillations or lattice distortions, alter the diffraction peak intensities from those predicted by the scattering factor.[63] Analysis of diffraction peak intensities can thus provide a simple method for probing disorder in the lattice. Consistent with the acTEM images, diffraction data (ESI section 2) shows that functionalisation by atomic oxygen results in similar disorder to functionalization by the modified Hummers' method and that chemical reduction and heating reduces lattice disorder but does not return the sheet to pristine graphene, all pointing to the ubiquity of ETDs in functionalized graphene and the challenges associated with removing them. This should be compared to the chemical composition determined by XPS which, as previously reported,[64] indicates that oxygen is

retained in reduced graphene oxide. Although it is natural to assume that the oxygen retained in rGO is associated with the ETDs, we cannot resolve the positions of the oxygen atoms from direct imaging. Instead, to understand whether oxygen functionalities are indeed preferentially retained in the structural defects, molecular dynamics simulations are used to investigate this hypothesis.

3.2 Interplay between Defects and Oxidation (Molecular Simulations). To explore the influence of the presence of ETDs on the retention and location of oxygen content in bwGO, molecular dynamics simulations were performed using the Reax force-field (ReaxFF),[55–57] based on a structural model of bwGO. The purpose of these simulations is not to re-create the conditions of the oxygen dosing experiments, but to probe how the hypothetical initial presence of ETDs might influence the retention of oxidative content after thermal treatment and indicate where this content is most likely located.

The key distinction between previous simulation studies[37–44] and the current work is that ETDs were introduced into our initial structures from the outset. Our experiments have shown that ETDs are an important feature of both bwGO and rGO, thus exploring the structural evolution of oxygen at these large defect sites via simulation will extend our understanding of GO in general. This decision to introduce ETDs into the initial structures for our simulations was informed by practicalities. The deliberate introduction of both ETDs and oxidative groups prior to annealing enables the study of the interaction between these two features, which are thought to co-exist prior to annealing, on timescales that are amenable to ReaxFF simulations. Details of the justification of this choice are provided in 'Model Justification', ESI section 3.

To isolate the effects of the different types of defects on oxygen retention, four different cases of graphene lattice were

considered, starting with the carbon lattice of GO sheet with no defects (GO-N). The GO-N model has been widely adopted as a basis of previously-reported MD simulations performed using ReaxFF, where no lattice defects have been induced prior to annealing. GO-N provides a broad point of comparison to these previous simulations, although the functional groups used to decorate the GO structure, as well as simulation times and temperatures, vary across studies. The novel feature of the current work is the consideration of three additional initial structural models devised here: GO with vacancy defects (holes), with topological defects (Stone-Wales defects and a "mini" grain boundary defect), and with both vacancy and topological defects (i.e. ETDs); these three cases are referred to as GO-V, GO-T and GO-TV, respectively. Holes and topological defect edges were pre-functionalized with oxygen-bearing groups, and the remainder of the oxygen content was initially distributed across randomly selected sites. These three models capture the hypothetical scenarios where the oxygen-bearing content has migrated from basal regions of the surface to become trapped at the edges of the different defect types. All four models were then subjected to computational thermal annealing protocols as detailed and justified in the Methods.

The introduction of vacancy defects, topological defects, and ETDs all enhanced loss of carbon from the lattice during the annealing process (Table S1, ESI), compared with the initially defect free case (GO-N), where the amount of lost carbon was not substantial (< 2%). Similar to our results for GO-N, previously-reported simulations of GO annealing (based on a GO-N-like structure) yielded minimal loss of carbon.[38] Carbon ejection was greatest for the GO-TV case at 2500 K, lost both via the edges of the existing defects and from the basal plane. In Figure 3, this can be observed visually with the appearance of holes in the post-annealed state. This suggests that the initial presence of ETDs can promote additional vacancy defects, which in turn may serve to retain oxygen content (as explained herein). In addition to the loss of carbon, the degree of deformation of the 2D carbon lattice in the 3rd dimension (perpendicular to the sheet plane) as a result of the annealing process was substantial (Figure S3, ESI).

However, not all of the newly-created holes were associated with carbon loss; some holes were created via an "unzipping" mechanism to form ruptures in the sheet. This unzipping mechanism appeared to be initiated by the presence of adjacent bridging oxygens, and is also supported by DFT studies.[31,32,65] At the atomic level, an epoxide oxygen atom rearranges to an ether type arrangement with cleavage of the C-C bond (Figure 4a), without any loss of carbon; a row of such groups rearranges to yield a linear rupture in the carbon sheet, which is held together by the oxygens (Figure 4b). When these bridging oxygen groups are subsequently lost (or converted) during annealing, the rupture in the carbon lattice remains. As illustrated in Figure 3, this was the sole mechanism for hole formation in GO-N. Therefore, vacancy defects appeared after annealing at 900 K, even for GO-N, where there is no loss of carbon. Previous ReaxFF simulations reported by Bagri *et al*. (which used the same ReaxFF potential as the current work) did not note any unzipping via ether groups during annealing,[37] and
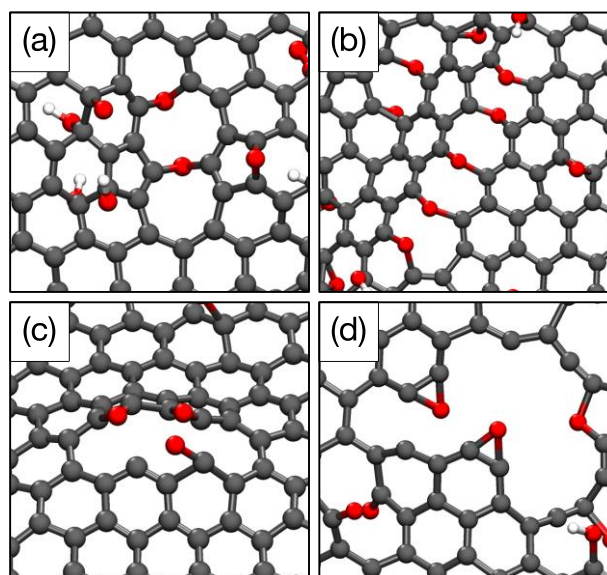

Figure 4. Four examples of structures of post-annealing oxygen retention at defect sites. Examples shown for (a-b) 900 K GO-T, (c) 1200 K GO-N, and (d) 1200 K GO-V. Red, white, and grey spheres indicate oxygen, hydrogen and the carbon atoms, respectively.

suggested that the relevant energy barrier was too high to be feasible. However, our observation of rupture could be due to a slower heating schedule used in the current work. These findings suggest that carbon loss is not a pre-requisite for lattice hole formation, even at relatively low annealing temperatures. These resultant holes are capable of trapping oxygen, as detailed here.

Compared with carbon retention, the initial presence of defects had the opposite effect on oxygen loss; introduction of lattice defects enhanced the retention of surface-attached oxygen during the annealing process, compared with GO-N, at all temperatures (Figure 5). As summarized in Figure 5a, although the amount of retained oxygen decreased as annealing temperature increased for all cases, the amount of oxygen retained for GO-N was always lowest. Figures 5b-d provide the post-annealing breakdown of total retained oxygen for hydroxyl, ether and carbonyl oxygens, respectively. Notably, the initial structures included only hydroxyl and epoxide groups, thus carbonyl groups have been generated during annealing. This result is consistent with a previous simulation study on the annealing of a graphene sheet decorated solely with epoxide groups, which resulted in the conversion of epoxies to either carbonyls or non-epoxide ether groups.[31] For all GO lattices under 2500 K, the number of hydroxyl and ether groups decreased with increasing annealing temperature whereas the number of carbonyl groups increased. However, GO-T, GO-V, and GO-TV supported the greatest retention of epoxies and the greatest chemical conversion into carbonyls. In particular, for ether and carbonyls the presence of topological defects (with or without vacancy defects, GO-T or GO-TV) enhanced this effect in the 900-1200 K range, relative to GO-V. In summary, substantive oxygen content was retained for the highest annealing temperature of 2500 K in all but the GO-N cases,
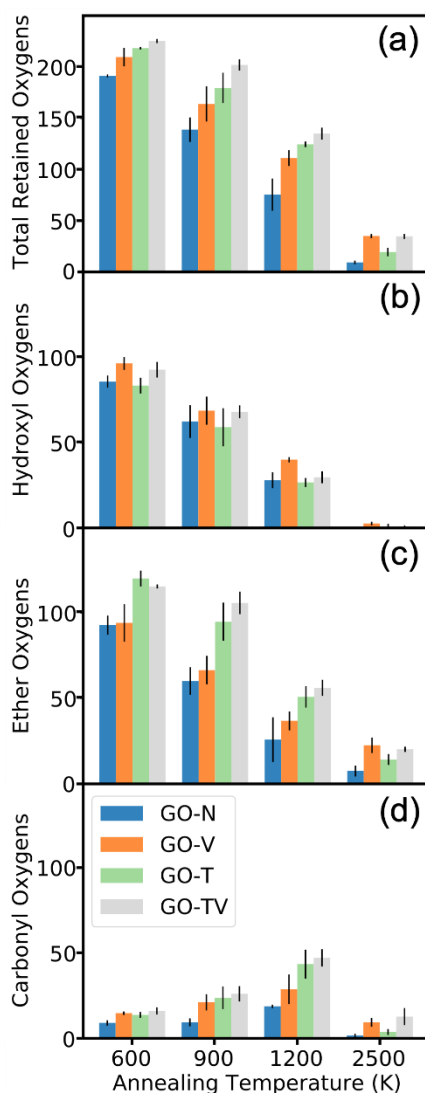
Figure 5. Predicted comparison of numbers of post-annealing surface-retained oxygens for the four types of GO initial state: defect free (GO-N), vacancy-defect (GO-V), topological-defect (GO-T), and topological-vacancy-defect (GO-TV) GO structures. Panel (a) shows the total number of retained oxygens in each case. Panels (b)–(d) indicate the breakdown in the number of retained oxygen in terms of hydroxyl, ether, and carbonyl, respectively.

suggesting it might not be possible to fully reduce GO, due to the presence of ETDs.

The outcomes of these molecular simulations are consistent with the experimental observations, namely in suggesting that retention of oxygen is most pronounced for graphene lattices that feature ETDs. However, these simulations also indicate the likely locations of this retained oxygen content, which is currently inaccessible to experimental approaches. The locations of the retained oxygen post-annealing was evaluated quantitatively (summarized in Table S2, ESI), by examining whether the remaining oxygen was bound to a defect carbon (defined as carbon atoms associated with either a vacancy defect, or a topological defect, or both) or the basal plane (defined as any non-defect carbon). As the annealing temperature increased, the proportion of total retained oxygen bound to a defect site, as opposed to the basal sites, increased

for all cases. This can be noted qualitatively in Figure 3, where in the initial case oxygen is spread over the basal plane, and at 900 K was still observed on the basal plane but with retention of oxygen on all defects, whereas at 1200 K the retained oxygen was strongly localized at the defect sites. Figure 4a illustrates the post-annealing 900 K structure where a Stone-Wales defect retained two bridging oxygen atoms (non-epoxide ether), as well as an epoxide and a di-hydroxyl; in Figure 4c and 4d, in examples taken from annealing at 1200 K, oxygen was retained at hole edges in the form of epoxide, carbonyl, and bridging oxygen groups. DFT calculations probing the stability of epoxide, carbonyl and non-epoxide ether groups on vacancy edges have been previously reported,[66] supporting the use of these ReaxFF annealed structures as a basis for analysis of the functional group composition at different temperatures.

For annealing at 2500 K, the proportion of total retained oxygen bound to defect carbons was >90% for all cases, and for the GO-TV case, none of the total retained oxygen remained bound to the basal plane (Table S2, ESI). The difference in locations of retained oxygen between the different cases was more pronounced at lower annealing temperatures, where the formation of new defects had not yet occurred. For example, at 600 K only 3% of the total retained oxygen was located on a defect carbon for the GO-N case; whereas for the GO-V, GO-T and GO-TV cases the proportion of the total retained oxygen situated on defect sites ranged from 24%-55%; additionally, the amount of total bound oxygen was 6-11% higher than the case where no defects were introduced.

In summary, by performing simulations without defects, with holes only, topological defects only, and ETDs, oxygen retention, location and functional group have been monitored as a function of defect type. These examples illustrate the overall finding that annealing could not eliminate all oxygen content, and that this oxygen retention was most pronounced when ETDs were initially present, which served to trap these oxygens and, in some instances, facilitate chemical conversion into carbonyl groups. These simulation findings support the hypothesis that the intrinsic presence of ETDs (regardless of their provenance) can strongly influence the properties of GO, such as the mechanical properties.

3.3 Mechanical properties of functionalized graphene. The effect of functionalization and structural disorder on the mechanical properties of graphene was studied both experimentally and computationally. An atomic force microscope was used to measure the elastic modulus and the breaking strength of freely suspended graphene films, in a similar geometry to that previously used to determine the mechanical properties of graphene.[51] Graphene films were supported on TEM grids containing an array of circular holes in a SiN membrane. To take statistically significant measurements, an automated procedure was employed to collect force curves (measuring the force as a function of indentation) from hundreds of holes across the sample. Each force curve was fit to obtain the elastic modulus of the films (summarized in the Methods) and to determine the breaking strength. The maximum indentation force that could be applied was 1.2 µN, placing an upper limit on the measurement of the breaking strength.

ARTICLE

Figure 6 summarises the mechanical response of the graphene membranes. Red diamonds on the plot show the breaking strength against the elastic modulus for 'pristine' CVD grown graphene. 82 % of these measurements lie on the line of maximum breaking strength, meaning most of the graphene film did not break up to the maximum force of 1.2 µN. The few points that lie below this line are likely to be from regions that contained defects such as grain boundaries in the CVD grown graphene film.[20] The average 2D elastic modulus for CVD graphene was determined to be 400±20 Nm^{-1}, which corresponds to a Young's modulus of 1.19±0.05 TPa. Both the high breaking strength and the Young's modulus are consistent with those expected of pristine graphene, which has a breaking strength of 42 Nm^{-1}, a 2D elastic modulus of 340 Nm^{-1} and a Young's modulus of 1.0 TPa.[51]

After dosing with atomic oxygen for two minutes, the dark green squares, the average Young's modulus decreases to 0.282±0.009 TPa and the average breaking strength to 0.38±0.02 µN. At this stage there is considerable variability in the breaking strength which is clearly strongly correlated to the Young's modulus, although the change in Young's modulus is smaller. This is consistent with heterogeneity in the levels of functionalisation. The mechanical properties are further decreased after four minutes exposure to atomic oxygen (light green crosses), with an average Young's modulus of 0.210±0.008 TPa and average breaking strength of 0.140±0.007 µN. Hence even low levels of functionalization significantly reduce the mechanical properties of graphene, decreasing both its stiffness and strength.

Mechanical measurements on aGO, blue rectangles in Figure 6, give an average 2D elastic modulus of 230 ± 10 N m^{-1} and an average breaking strength of 0.45 ± 0.02 µN, a clear reduction in the mechanical performance compared to graphene. To compare this to literature values, we assume a thickness of 1 nm to give a Young's modulus of 0.230 ± 0.010 TPa, consistent with previous AFM measurements[67] and with investigations of GO in composites.[68,69] Note that the dramatic decrease in Young's modulus from graphene to graphene oxide is due to both a decrease in the 2D elastic modulus and a significant increase in thickness of the GO monolayers. The statistically significant number of mechanical measurements made here allow further insight. There is a much larger spread in both Young's modulus and breaking strength for GO, with a strong correlation between them. We attribute this to two factors: the structure of GO is heterogeneous at the nanoscale; and the GO membranes are not uniformly flat monolayers, some areas of the grids may contain multiple GO flakes stacked on top of each other and there may be some folds or wrinkles.

After chemical reduction to rGO, purple circles in Figure 6, the mechanical properties do not become closer to pristine graphene but rather remain similar to those of aGO. The average values, 170±10 Nm^{-1} for the 2D elastic modulus and 0.34±0.02 µN for the breaking strength, show a small decrease relative to GO and again a similar spread in the results is observed, with a clear correlation between breaking strength and Young's modulus. We attribute the small difference in the average values relative to aGO to be due to small differences in
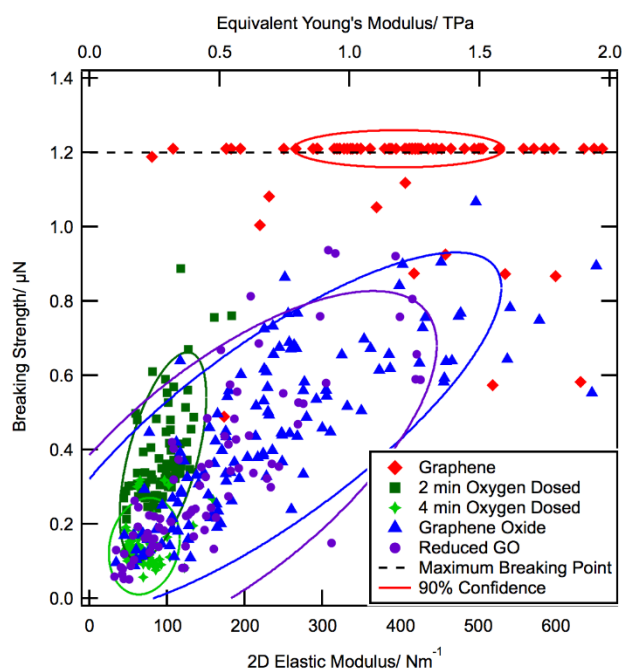

Figure 6. Scatter plot of all the breaking loads and elastic moduli of the tested graphene and functionalised graphene samples. Each data point corresponds to measurements on a separate section of suspended graphene membrane. The ellipses correspond to 90% confidence intervals for each data set and demonstrate the correlation between breaking strength and elastic modulus. The black dashed line corresponds to the maximum breaking strength that could be measured, the points just above that line correspond to graphene membranes that did not break up to that point. The equivalent Young's modulus is calculated assuming a 0.335 nm film thickness, corresponding to graphene.

the uniformity of the GO monolayers in each sample: the mechanical properties of aGO and rGO are very similar.

The data from mechanical measurements thus show that even mild chemical functionalization can severely degrade the mechanical properties of graphene, apparent both from measurements on controlled gas phase functionalised graphene and wet chemical functionalised graphene (GO). In both, there are significant variations in mechanical properties consistent with heterogeneity in the structure at the nanoscale. The similarity between the average mechanical properties of aGO and rGO is instructive. Chemical reduction will have significantly decreased the density of epoxide and hydroxide functional groups but will not have altered the density of extended topological defects or oxygen groups associated with vacancies, suggesting that these play a critical role in preventing the recovery of the mechanical properties of pristine graphene. Molecular dynamics simulations of the mechanical properties of both pristine graphene and annealed GO structures were performed and found to be consistent with these findings. ReaxFF MD simulations have been previously used to study the mechanical properties of GO structures which feature a minor amount of topological or point vacancy defects.[39,70,71] These simulations were not intended to be exhaustive, but rather to illustrate differences in the mechanical properties between structures with more or less numbers of ETDs. Stress-strain simulations at 300 K were used to predict Young's modulus for pristine graphene (PG), and the GO-N and GO-V structures

following annealing at both 600 K and 1200 K. The latter were considered to probe whether the amount of defect-retained oxygen influenced the mechanical properties. As an additional check of Young's modulus, the elastic constants of the sheets were also calculated at 0 K, based on the second-derivatives of the potential energy with respect to atomic position. Regardless of the annealing temperature used to prepare the sample, and the procedure used to calculate Young's modulus, the same trend was identified, namely that E(PG)>E(GO-N)>E(GO-V), consistent with the experimental results (simulation data in Figure S4, ESI). Previously calculated values for the Young's modulus of PG and GO-N range from 1.04-1.39 TPa [72–74] and 0.2-0.8 TPa [75,76], respectively. Here, the Young's modulus of graphene was calculated to be 0.71/0.94 TPa for the stress-strain simulations and elastic constant calculations respectively. Values for GO-N samples annealed at 600 K and 1200 K were 0.39 TPa and 0.37 TPa respectively for the stress-strain simulations, in line with the previously published estimates mentioned above. Analogous values from the elastic constant calculations were similar to their stress-strain counterparts in each case (Figure S4, ESI). The related 2D Young's modulus values are also summarised in Figure S4 and are consistent with previously reported values for graphene.[77] These findings further support the hypothesis that the presence of both residual oxygen content and vacancy defects, which remain even after GO reduction, serve to irreversibly compromise the mechanical integrity of rGO and hrGO.

Conclusions

Our results demonstrate that oxygen functionalization of graphene directly causes structural changes to the graphene basal plane that are not removed by reduction methods. Extended topological defects were observed both in graphene oxide produced by a conventional modified Hummers' method, and by controlled functionalization of pristine graphene by exposure to atomic oxygen under ultrahigh vacuum. For the latter, even though low-levels of oxygen functionalization by exposure to atomic oxygen are known to be reversible with no damage to the graphene lattice,[16,58] exposure for longer times results in an oxidised and defective structure similar to GO produced by conventional wet-chemical methods. Our data add compelling evidence that the ETDs are introduced during the functionalization process, rather than only during the reduction process, and should be expected to be ubiquitous in all but the most minimally functionalized graphene. Molecular dynamics simulations indicated that after reduction/annealing, the retained oxygen groups are preferentially associated with the extended topological defect structures. Subsequent reduction may remove oxygenation but has no effect upon the extended defect structures. The binding of other atoms such as hydrogen and fluorine at the defect sites of graphene oxide has been shown to be significantly stronger than that on the basal plane[78] which supports the notion that without defect removal they are irreversibly bound. Further, it has been shown with other functional groups that the agglomeration of groups that can occur can further strengthen the binding.[79] We suggest that the interplay of functional groups binding on defect sites, and the defect sites providing a site of agglomeration, both enhance the binding to such a degree that the groups are irremovable upon reduction. Thus, as an exemplar, by combining molecular dynamics simulations and mechanical measurements, we illustrated how functionalization significantly deteriorated the mechanical properties of graphene through the introduction of extended topological defects and how reduction was unable to restore these properties.

Graphene oxide is a term used to refer to a family of materials formed from the oxidation and exfoliation of graphite to monolayer oxygen functionalized sheets. The physical and chemical structure of these materials varies depending on the protocols followed to produce them. But from the comparative study given here between wet-chemical and gas-phase functionalization, we can extend the existing and widely-accepted structural models of GO, to summarize the key categories of features present to a greater or lesser extent in all graphene oxides: (1) on-plane oxygen functional groups, including ether and hydroxyl, in regions where the hexagonal carbon lattice is retained, as described by the Lerf-Klinowski model; (2) oxidative debris adhered to the as-produced graphene oxide, containing high concentrations of oxygen functional groups; (3) extended topological defects in the carbon lattice, with associated oxygen functional groups, such as carbonyls, that are more stable due to their association with the vacancy structures. Whilst there are also oxygen atoms associated with sheet edges, these correspond to only a small fraction of the material (typically < 0.1%) and so are unlikely to contribute significantly to the macroscopic properties. In summary, this work emphasizes the importance of extended topological defects as a ubiquitous trait common to all graphene oxides, regardless of their provenance, and their central role to understanding the atomic structure, chemical properties, and physical properties of graphene oxide.

Author Contributions

Conceptualization: NRW, JPR, TRW
Methodology: NAG, FV, HJ, AJM, HRT, MW, MS, MH, NRW
Software: NAG, FV
Validation: NAG, FV, TRW, NRW, JPR, AJM, HRT, MW, MS, MH, RSE
Formal analysis: NAG, FV, TRW, AJM, HRT, MS, MH, NRW
Investigation: NAG, FV, HJ, AJM, HRT, MW, MS, MH, NRW
Resources: TRW, JPR, NRW
Data Curation: NAG, FV, HJ, AJM, HRT, MW, MS, MH
Writing – Original Draft: TRW, JPR, NRW, AJM
Writing – Review and Editing: all authors
Visualisation: NAG, FV, AJM, NRW, MS
Supervision: TRW, JPR, NRW
Project Administration: TRW, JPR, NRW
Funding Acquisition: TRW, JPR, NRW

Conflicts of interest

There are no conflicts to declare.

Acknowledgements

References

1   A. K. Geim and K. S. Novoselov, The rise of graphene., *Nat. Mater.*, 2007, **6**, 183–91.

2   A. C. Ferrari, F. Bonaccorso, V. Fal'ko, K. S. Novoselov, S. Roche, P. Bøggild, S. Borini, F. H. L. Koppens, V. Palermo, N. Pugno, J. a. Garrido, R. Sordan, A. Bianco, L. Ballerini, M. Prato, E. Lidorikis, J. Kivioja, C. Marinelli, T. Ryhänen, A. Morpurgo, J. N. Coleman, V. Nicolosi, L. Colombo, A. Fert, M. Garcia-Hernandez, A. Bachtold, G. F. Schneider, F. Guinea, C. Dekker, M. Barbone, Z. Sun, C. Galiotis, A. N. Grigorenko, G. Konstantatos, A. Kis, M. Katsnelson, L. Vandersypen, A. Loiseau, V. Morandi, D. Neumaier, E. Treossi, V. Pellegrini, M. Polini, A. Tredicucci, G. M. Williams, B. Hee Hong, J.-H. Ahn, J. Min Kim, H. Zirath, B. J. van Wees, H. van der Zant, L. Occhipinti, A. Di Matteo, I. a. Kinloch, T. Seyller, E. Quesnel, X. Feng, K. Teo, N. Rupesinghe, P. Hakonen, S. R. T. Neil, Q. Tannock, T. Löfwander and J. Kinaret, Science and technology roadmap for graphene, related two-dimensional crystals, and hybrid systems, *Nanoscale*, 2015, **7**, 4598–4810.

3   S. Stankovich, D. A. Dikin, R. D. Piner, K. A. Kohlhaas, A. Kleinhammes, Y. Jia, Y. Wu, S. T. Nguyen and R. S. Ruoff, Synthesis of graphene-based nanosheets via chemical reduction of exfoliated graphite oxide, *Carbon N. Y.*, 2007, **45**, 1558–1565.

4   Y. Hernandez, V. Nicolosi, M. Lotya, F. M. Blighe, Z. Sun, S. De, I. T. McGovern, B. Holland, M. Byrne, Y. K. Gun'Ko, J. J. Boland, P. Niraj, G. Duesberg, S. Krishnamurthy, R. Goodhue, J. Hutchison, V. Scardaci, A. C. Ferrari and J. N. Coleman, High-yield production of graphene by liquid-phase exfoliation of graphite, *Nat. Nanotechnol.*, 2008, **3**, 563–568.

5   D. R. Dreyer, S. Park, C. W. Bielawski and R. S. Ruoff, The chemistry of graphene oxide., *Chem. Soc. Rev.*, 2010, **39**, 228–40.

6   S. Eigler and A. Hirsch, Chemistry with graphene and graphene oxide - Challenges for synthetic chemists, *Angew. Chemie - Int. Ed.*, 2014, **53**, 7720–7738.

7   D. R. Dreyer, A. D. Todd and C. W. Bielawski, Harnessing the chemistry of graphene oxide, *Chem. Soc. Rev.*, 2014, **43**, 5288.

8   T. Nakajima, A. Mabuchi and R. Hagiwara, A new structure model of graphite oxide, *Carbon N. Y.*, 1988, **26**, 357–361.

9   H. He, J. Klinowski, M. Forster and A. Lerf, A new structural model for graphite oxide, *Chem. Phys. Lett.*, 1998, **287**, 53–56.

10   A. Lerf, H. He, M. Forster and J. Klinowski, Structure of Graphite Oxide Revisited ‖, *J. Phys. Chem. B*, 1998, **102**, 4477–4482.

11   T. Szabó, O. Berkesi, P. Forgó, K. Josepovits, Y. Sanakis, D. Petridis and I. Dékány, Evolution of surface functional groups in a series of progressively oxidized graphite oxides, *Chem. Mater.*, 2006, **18**, 2740–2749.

12   P. Feicht and S. Eigler, Defects in Graphene Oxide as Structural Motifs, *ChemNanoMat*, 2018, **4**, 244–252.

13   J. P. Rourke, P. A. Pandey, J. J. Moore, M. Bates, I. A. Kinloch, R. J. Young and N. R. Wilson, The real graphene oxide revealed: Stripping the oxidative debris from the graphene-like sheets, *Angew. Chemie - Int. Ed.*, 2011, **50**, 3173–3177.

14   H. R. Thomas, S. P. Day, W. E. Woodru, C. Valle, R. J. Young, I. A. Kinloch, G. W. Morley, J. V Hanna, N. R. Wilson and J. P. Rourke, Deoxygenation of Graphene Oxide: Reduction or Cleaning?, *Chem. Mater.*, 2013, 3580–3588.

15   A. J. Stone and D. J. Wales, Theoretical studies of icosahedral C60 and some related species, *Chem. Phys. Lett.*, 1986, **128**, 501–503.

16   A. J. Marsden, P. Brommer, J. J. Mudd, M. A. Dyson, R. Cook, M. Asensio, J. Avila, A. Levy, J. Sloan, D. Quigley, G. R. Bell and N. R. Wilson, Effect of oxygen and nitrogen functionalization on the physical and electronic structure of graphene, *Nano Res.*, 2015, **8**, 2620–2635.

17   C. Gómez-Navarro, J. C. Meyer, R. S. Sundaram, A. Chuvilin, S. Kurasch, M. Burghard, K. Kern, U. Kaiser, C. Gómez-Navarro, J. C. Meyer, R. S. Sundaram, A. Chuvilin, S. Kurasch, M. Burghard, K. Kern and U. Kaiser, Atomic Structure of Reduced Graphene Oxide, *Nano Lett.*, 2010, **10**, 1144–1148.

18   B. K. Erickson, R. Erni, Z. Lee, N. Alem, W. Gannett, A. Zettl, K. Erickson, R. Erni, Z. Lee, N. Alem, W. Gannett and A. Zettl, Determination of the Local Chemical Structure of Graphene Oxide and Reduced Graphene Oxide, *Adv. Mater.*, 2010, **22**, 4467–4472.

19   S. H. Dave, C. Gong, A. W. Robertson, J. H. Warner and J. C. Grossman, Chemistry and Structure of Graphene Oxide via Direct Imaging, *ACS Nano*, 2016, **10**, 7515–7522.

20   P. Y. Huang, C. S. Ruiz-Vargas, A. M. van der Zande, W. S. Whitney, M. P. Levendorf, J. W. Kevek, S. Garg, J. S. Alden, C. J. Hustedt, Y. Zhu, J. Park, P. L. McEuen and D. a Muller, Grains and grain boundaries in single-layer graphene atomic patchwork quilts., *Nature*, 2011, **469**, 389–92.

21   F. Grote, C. Gruber, F. Börrnert, U. Kaiser and S. Eigler, Thermal Disproportionation of Oxo-Functionalized Graphene, *Angew. Chemie - Int. Ed.*, 2017, **56**, 9222–9225.

22   M. Pelaez-Fernandez, A. Bermejo, A. M. Benito, W. K. Maser and R. Arenal, Detailed thermal reduction analyses of Graphene Oxide via in-situ TEM/EELS studies, *Carbon N. Y.*, 2021, 104743.

23   K. A. Mkhoyan, A. W. Contryman, J. Silcox, D. A. Stewart, G. Eda, C. Mattevi, S. Miller and M. Chhowalla, Atomic and Electronic Structure of Graphene-Oxide, *Nano Lett.*, 2009, **9**, 1058–1063.

24   D. Zhu, H. Pu, P. Lv, Z. Zhu, C. Yang, R. Zheng, Z. Wang, C.

Liu, E. Hu, J. Zheng, K. Yu, W. Wei, L. Chen and J. Chen, Healing of reduced graphene oxide with methane + hydrogen plasma, *Carbon N. Y.*, 2017, **120**, 274–280.

25   V. López, R. S. Sundaram, C. Gómez-Navarro, D. Olea, M. Burghard, J. Gómez-Herrero, F. Zamora and K. Kern, Chemical Vapor Deposition Repair of Graphene Oxide: A Route to Highly-Conductive Graphene Monolayers, *Adv. Mater.*, 2009, **21**, 4683–4686.

26   O. C. Compton and S. T. Nguyen, Graphene Oxide, Highly Reduced Graphene Oxide, and Graphene: Versatile Building Blocks for Carbon-Based Materials, *Small*, 2010, **6**, 711–723.

27   K. K. H. De Silva, H. H. Huang, R. Joshi and M. Yoshimura, Restoration of the graphitic structure by defect repair during the thermal reduction of graphene oxide, *Carbon N. Y.*, 2020, **166**, 74–90.

28   M. Cheng, R. Yang, L. Zhang, Z. Shi, W. Yang, D. Wang, G. Xie, D. Shi and G. Zhang, Restoration of graphene from graphene oxide by defect repair, *Carbon N. Y.*, 2012, **50**, 2581–2587.

29   C. Mattevi, G. Eda, S. Agnoli, S. Miller, K. A. Mkhoyan, O. Celik, D. Mastrogiovanni, G. Granozzi, E. Carfunkel and M. Chhowalla, Evolution of electrical, chemical, and structural properties of transparent and conducting chemically derived graphene thin films, *Adv. Funct. Mater.*, 2009, **19**, 2577–2583.

30   X. Gao, J. Jang and S. Nagase, Hydrazine and Thermal Reduction of Graphene Oxide: Reaction Mechanisms, Product Structures, and Reaction Design, *J. Phys. Chem. C*, 2010, **114**, 832–842.

31   T. Sun and S. Fabris, Mechanisms for Oxidative Unzipping and Cutting of Graphene, *Nano Lett.*, 2012, **12**, 17–21.

32   Y. Yamada, H. Yasuda, K. Murota, M. Nakamura, T. Sodesawa and S. Sato, Analysis of heat-treated graphite oxide by X-ray photoelectron spectroscopy, *J. Mater. Sci.*, 2013, **48**, 8171–8198.

33   P. Sun, Y. Wang, H. Liu, K. Wang, D. Wu, Z. Xu and H. Zhu, Structure Evolution of Graphene Oxide during Thermally Driven Phase Transformation: Is the Oxygen Content Really Preserved?, *PLoS One*, 2014, **9**, e111908.

34   D. D'Angelo, C. Bongiorno, M. Amato, I. Deretzis, A. La Magna, E. Fazio and S. Scalese, Oxygen Functionalities Evolution in Thermally Treated Graphene Oxide Featured by EELS and DFT Calculations, *J. Phys. Chem. C*, 2017, **121**, 5408–5414.

35   C. Li, X. Chen, L. Shen and N. Bao, Revisiting the Oxidation of Graphite: Reaction Mechanism, Chemical Stability, and Structure Self-Regulation, *ACS Omega*, 2020, **5**, 3397–3404.

36   E. Chigo Anota, A. Escobedo-Morales, M. Salazar Villanueva, O. Vázquez-Cuchillo and E. Rubio Rosas, On the influence of point defects on the structural and electronic properties of graphene-like sheets: a molecular simulation study, *J. Mol. Model.*, 2013, **19**, 839–846.

37   A. Bagri, C. Mattevi, M. Acik, Y. J. Chabal, M. Chhowalla and V. B. Shenoy, Structural evolution during the reduction of chemically derived graphene oxide, *Nat. Chem.*, 2010, **2**, 581–587.

38   L.-C. C. Lin and J. C. Grossman, Atomistic understandings of reduced graphene oxide as an ultrathin-film nanoporous membrane for separations, *Nat. Commun.*, 2015, **6**, 8335.

39   X. Liu and Q. Yang, Molecular dynamic simulation of mechanical behaviour of RGO produced by thermal reduction method, *Micro Nano Lett.*, 2017, **12**, 638–642.

40   F. Raffone, F. Savazzi and G. Cicero, Molecular dynamics study of the pore formation in single layer graphene oxide by a thermal reduction process, *Phys. Chem. Chem. Phys.*, 2021, **23**, 11831–11836.

41   A. Antidormi, S. Roche and L. Colombo, Impact of oxidation morphology on reduced graphene oxides upon thermal annealing, *J. Phys. Mater.*, 2019, **3**, 015011.

42   Z. Yang, Y. Sun, F. Ma, Y. Lu and T. Zhao, Pyrolysis mechanisms of graphene oxide revealed by ReaxFF molecular dynamics simulation, *Appl. Surf. Sci.*, 2020, **509**, 145247.

43   J. Chen and L. Li, Effect of oxidation degree on the thermal properties of graphene oxide, *J. Mater. Res. Technol.*, 2020, **9**, 13740–13748.

44   Q. Qiao, C. Liu, W. Gao and L. Huang, Graphene oxide model with desirable structural and chemical properties, *Carbon N. Y.*, 2019, **143**, 566–577.

45   N. R. Wilson, A. J. Marsden, M. Saghir, C. J. Bromley, R. Schaub, G. Costantini, T. W. White, C. Partridge, A. Barinov, P. Dudin, A. M. Sanchez, J. J. Mudd, M. Walker and G. R. Bell, Weak mismatch epitaxy and structural Feedback in graphene growth on copper foil, *Nano Res.*, 2013, **6**, 99–112.

46   W. S. Hummers and R. E. Offeman, Preparation of Graphitic Oxide, *J. Am. Chem. Soc.*, 1958, **80**, 1339–1339.

47   N. R. Wilson, P. A. Pandey, R. Beanland, R. J. Young, I. A. Kinloch, L. Gong, Z. Liu, K. Suenaga, J. P. Rourke, S. J. York and J. Sloan, Graphene Oxide: Structural Analysis and Application as a Highly Transparent Support for Electron Microscopy, *ACS Nano*, 2009, **3**, 2547–2556.

48   H. A. Becerril, J. Mao, Z. Liu, R. M. Stoltenberg, Z. Bao and Y. Chen, Evaluation of Solution-Processed Reduced Graphene Oxide Films as Transparent Conductors, *ACS Nano*, 2008, **2**, 463–470.

49   P. A. Pandey, N. R. Wilson and J. A. Covington, Pd-doped reduced graphene oxide sensing films for H2 detection, *Sensors Actuators B Chem.*, 2013, **183**, 478–487.

50   J. E. Sader, J. W. M. Chon and P. Mulvaney, Calibration of rectangular atomic force microscope cantilevers, *Rev. Sci. Instrum.*, 1999, **70**, 3967–3969.

51   C. Lee, X. Wei, J. W. Kysar and J. Hone, Measurement of the Elastic Properties and Intrinsic Strength of Monolayer Graphene, *Science (80-.).*, 2008, **321**, 385–388.

52   N. A. Marks, M. F. Cover and C. Kocer, Simulating temperature effects in the growth of tetrahedral amorphous carbon: The importance of infrequent events, *Appl. Phys. Lett.*, 2006, **89**, 131924.

53   C. de Tomas, I. Suarez-Martinez, F. Vallejos-Burgos, M. J. López, K. Kaneko and N. A. Marks, Structural prediction of graphitization and porosity in carbide-derived carbons, *Carbon N. Y.*, 2017, **119**, 1–9.

54   S. Plimpton, Fast Parallel Algorithms for Short-Range Molecular Dynamics, *J. Comput. Phys.*, 1995, **117**, 1–19.

55   A. C. T. van Duin, S. Dasgupta, F. Lorant and W. A. Goddard, ReaxFF: A Reactive Force Field for Hydrocarbons, *J. Phys. Chem. A*, 2001, **105**, 9396–9409.

56   K. Chenoweth, A. C. T. van Duin and W. A. Goddard, ReaxFF Reactive Force Field for Molecular Dynamics Simulations of Hydrocarbon Oxidation, *J. Phys. Chem. A*, 2008, **112**, 1040–1053.

57   R. Smith, K. Jolley, C. Latham, M. Heggie, A. van Duin, D. van Duin and H. Wu, A ReaXFF carbon potential for radiation damage studies, *Nucl. Instruments Methods Phys. Res. Sect. B Beam Interact. with Mater. Atoms*, 2017, **393**, 49–53.

58   K. Chenoweth, A. C. T. van Duin, W. A. Goddard, O. Seri-Livni, C. Saguy, F. Horani, E. Lifshitz, D. Cheskis, R. Smith, K. Jolley, C. Latham, M. Heggie, A. C. T. van Duin, D. van Duin, H. Wu, S. Plimpton, A. C. T. van Duin, S. Dasgupta, F. Lorant, W. A. Goddard, A. C. Ferrari, D. M. Basko, B. Shevitski, M. Mecklenburg, W. A. Hubbard, E. R. White, B. Dawson, M. S. Lodge, M. Ishigami, B. C. Regan, S. H. Dave, C. Gong, A. W. Robertson, J. H. Warner, C. Grossman, M. M. Z. Hossain, J. E. J. Johns, K. H. K. K. H. Bevan, H. J. Karmel, Y. T. Liang, S. Yoshimoto, K. Mukai, T. Koitaya, J. Yoshinobu, M. Kawai, A. M. Lear, L. L. Kesmodel, S. L. Tait, M. C. Hersam, J. C. Meyer, R. S. Sundaram, A. Chuvilin, S. Kurasch, M. Burghard, K. Kern, U. Kaiser, P. Feicht and S. Eigler, Chemically homogeneous and thermally reversible oxidation of epitaxial graphene., *Nat. Chem.*, 2012, **4**, 305–9.

59   A. C. Ferrari and D. M. Basko, Raman spectroscopy as a versatile tool for studying the properties of graphene, *Nat. Nanotechnol.*, 2013, **8**, 235–246.

60   G. Algara-Siller, O. Lehtinen, A. Turchanin and U. Kaiser, Dry-cleaning of graphene, *Appl. Phys. Lett.*, 2014, **104**, 153115.

61   P. Swift, Adventitious carbon - the panacea for energy referencing?, *Surf. Interface Anal.*, 1982, **4**, 47–51.

62   O. Seri-Livni, C. Saguy, F. Horani, E. Lifshitz and D. Cheskis, Effective Reduction of Oxygen Debris in Graphene Oxide, *Phys. Status Solidi Basic Res.*, 2020, **2000505**, 1–8.

63   B. Shevitski, M. Mecklenburg, W. A. Hubbard, E. R. White, B. Dawson, M. S. Lodge, M. Ishigami and B. C. Regan, Dark-field transmission electron microscopy and the Debye-Waller factor of graphene, *Phys. Rev. B*, 2013, **87**, 045417.

64   S. Pei and H.-M. Cheng, The reduction of graphene oxide, *Carbon N. Y.*, 2012, **50**, 3210–3228.

65   J.-L. Li, K. N. Kudin, M. J. McAllister, R. K. Prud'homme, I. A. Aksay and R. Car, Oxygen-Driven Unzipping of Graphitic Materials, *Phys. Rev. Lett.*, 2006, **96**, 176101.

66   X. Qi, X. Guo and C. Zheng, Density functional study the interaction of oxygen molecule with defect sites of graphene, *Appl. Surf. Sci.*, 2012, **259**, 195–200.

67   J. W. Suk, R. D. Piner, J. An and R. S. Ruoff, Mechanical Properties of Monolayer Graphene Oxide, *ACS Nano*, 2010, **4**, 6557–6564.

68   D. G. Papageorgiou, I. A. Kinloch and R. J. Young, Mechanical properties of graphene and graphene-based nanocomposites, *Prog. Mater. Sci.*, 2017, **90**, 75–127.

69   R. J. Young, I. A. Kinloch, L. Gong and K. S. Novoselov, The mechanics of graphene nanocomposites: A review, *Compos. Sci. Technol.*, 2012, **72**, 1459–1476.

70   A. Verma and A. Parashar, Reactive force field based atomistic simulations to study fracture toughness of bicrystalline graphene functionalised with oxide groups, *Diam. Relat. Mater.*, 2018, **88**, 193–203.

71   A. Verma and A. Parashar, Molecular dynamics based simulations to study the fracture strength of monolayer graphene oxide, *Nanotechnology*, 2018, **29**, 115706.

72   A. G. Kvashnin, P. B. Sorokin and D. G. Kvashnin, The Theoretical Study of Mechanical Properties of Graphene Membranes, *Fullerenes, Nanotub. Carbon Nanostructures*, 2010, **18**, 497–500.

73   M. M. Shokrieh and R. Rafiee, Prediction of Young's modulus of graphene sheets and carbon nanotubes using nanoscale continuum mechanics approach, *Mater. Des.*, 2010, **31**, 790–795.

74   Y. G. Yanovsky, E. A. Nikitina, Y. N. Karnet and S. M. Nikitin, Quantum mechanics study of the mechanism of deformation and fracture of graphene, *Phys. Mesomech.*, 2009, **12**, 254–262.

75   A. R. Khoei and M. S. Khorrami, Mechanical properties of graphene oxide: A molecular dynamics study, *Fullerenes, Nanotub. Carbon Nanostructures*, 2016, **24**, 594–603.

76   X. Zhang, S. Liu, H. Liu, J. Zhang and X. Yang, Molecular dynamics simulation of the mechanical properties of multilayer graphene oxide nanosheets, *RSC Adv.*, 2017, **7**, 55005–55011.

77   D. Akinwande, C. J. Brennan, J. S. Bunch, P. Egberts, J. R. Felts, H. Gao, R. Huang, J.-S. Kim, T. Li, Y. Li, K. M. Liechti, N. Lu, H. S. Park, E. J. Reed, P. Wang, B. I. Yakobson, T. Zhang, Y.-W. Zhang, Y. Zhou and Y. Zhu, A review on mechanics and mechanical properties of 2D materials—Graphene and beyond, *Extrem. Mech. Lett.*, 2017, **13**, 42–77.

78   P. A. Denis and F. Iribarne, Comparative Study of Defect Reactivity in Graphene, *J. Phys. Chem. C*, 2013, **117**, 19048–19055.

79   P. A. Denis and F. Iribarne, Cooperative behavior in functionalized graphene: Explaining the occurrence of 1,3 cycloaddition of azomethine ylides onto graphene, *Chem. Phys. Lett.*, 2012, **550**, 111–117.